Clean Technologies and Recycling

Clean Technologies and Recycling, 6 (1): 33–55.
DOI: 10.3934/ctr.2026002
Received: 29 September 2025
Revised: 09 December 2025
Accepted: 12 December 2025
Published: 07 January 2026

https://www.aimspress.com/journal/ctr

Research article

Performance improvement of lead-free $CsSnCl_3$-based perovskite solar cell using multiple ETLs: A SCAPS-1D simulation study

Rony Tota[1], Tarikul Islam Tasin[1], Md. Morsalin[1,*], Ragab A. Sayed[2,*], Sheeraz Iqbal[3,4], Shak Mahmudul Hasan[1], Md. Zamil Sultan[1] and Md. Muien Ahmed Arnob[1]

[1] Department of Electrical and Electronic Engineering, Hajee Mohammad Danesh Science and Technology University, Dinajpur, Bangladesh
[2] Automotive and Tractors Technology Department, Faculty of Technology and Education, Capital University – Helwan Branch, Cairo, Egypt
[3] Interdisciplinary Research Center for Sustainable Energy Systems, Research and Innovation, King Fahd University of Petroleum & Minerals, Dhahran 31261, Saudi Arabia
[4] Department of Electrical Engineering, University of Azad Jammu and Kashmir, 13100 Muzaffarabad, Pakistan

* **Correspondence:** Email: mdmorsalin.hstu@gmail.com; ragab.mahmoud@techedu.helwan.edu.eg.

Abstract: Cesium tin chloride ($CsSnCl_3$) is a potential and ecologically safe material for lead-free perovskite solar cells (PSCs). $CsSnCl_3$ is a strong candidate for sustainable energy applications due to its affordability, high energy efficiency, and excellent thermal stability. We simulated various $CsSnCl_3$ device structures with different electron transport layers (ETLs)—viz. WS_2, C60, and ZnSe—in combination with CBTS as the hole-transport layer (HTL), using the one-dimensional solar cell capacitance simulator (SCAPS-1D). We quantitatively evaluated the influence of the absorber layer thickness, doping concentration, defect density, and characteristics of the ETL and HTL on relevant photovoltaic (PV) parameters, such as power conversion efficiency (PCE) (η), short-circuit current density (J_{SC}), open-circuit voltage (V_{OC}), and fill factor (FF). The findings revealed that the choice of ETL has a great impact on the performance of the device. WS_2, C60, and ZnSe led to the highest PCEs at 22.09%, 19.94%, and 21.80%. Then, the effect of other factors was investigated, including capacitance-voltage behavior, interface defect, Mott–Schottky behavior, current density-voltage (J-V), quantum efficiency (QE), and recombination rates. The results were compared with the earlier research conducted on $CsSnCl_3$-based PSCs to assess enhancements and long-term sustainability. To summarize, this paper proposes the most effective and high-performance device configurations in lead-free

$CsSnCl_3$-based PSCs, as part of developing sustainable and cost-effective PV technologies.

Keywords: Lead-free PSCs; $CsSnCl_3$; SCAPS-1D; CBTS as HTL; different ETLs

1. Introduction

Conventional sources of energy, such as gas, oil, and coal, are greatly dependent upon to supply considerable energy requirements; however, they have adverse effects on the environment and cause climate change [1], and these resources are finite. As such, researchers have continuously focused on how to move away from these traditional sources of energy to renewable energy sources, including hydropower, solar, and wind energy. Solar energy is a highly abundant energy source; it greatly surpasses all the other renewable sources of energy combined [2]. Production of solar energy can definitely fulfil the energy requirements of humanity, even in the most high-tech societies. Nonetheless, solar energy needs to be collected, extracted, and stored to overcome the problem of daily fluctuations. The major components used to capture this are PV cells, which convert light into electricity. A third-generation PV cell, termed perovskite, promises to be able to compete with conventional solar technologies, being easier to manufacture and less costly to produce [3]. A popular solar cell (SC) design is the one-dimensional n-i-p flat heterojunction, a heterojunction built of several layers of semiconductors.

Of particular interest are perovskite solar cells (PSCs) due to their high efficiency and cost-effectiveness in converting solar energy [4]. Although lead-based PSCs present high efficiency, the issue of lead toxicity has prompted scientists to explore lead-free PSCs [5–7]. Halide perovskites are materials characterized by the formula ABX_3 [8], where "A" represents monovalent cations [Cs^+, $CH_3NH_3^+$, $CH(NH_2)_3^+$], "B" denotes cationic metals like Sn^{2+} or Pb^{2+}, and "X" corresponds to halogen ions (Cl^-, I^-, Br^-). $MAPbI_3$ (methylammonium lead triiodide) stands out as the predominant perovskite material utilized in SCs. A prospective contender is $CsSnCl_3$ as the perovskite absorber layer, which has been demonstrated to be highly efficient without the inclusion of lead [9]. Another material under consideration as PSC is cesium tin chloride ($CsSnCl_3$), a lead-free material of special interest.

PSCs have become a promising technology in the efficient conversion of energy at low cost. Traditionally, $CsSnCl_3$ and WS_2 have been used as electron transport layers (ETLs) and CBTS as the hole-transport layer (HTL) to increase performance. The bulk defect density of the absorber layer is determined to a large extent by the efficiency of such solar cells and can be tuned to achieve maximum performance. To further examine the effects of bulk defect density, scientists have employed simulation packages such as SCAPS to test the behavior of solar cells under various conditions [10,11]. These simulations enhance the efficiency and stability of PSCs for better application in renewable energy.

The performance of the $CsSnCl_3$-based PSC can be efficiently tested by changing the density of the defects (Nt) of the active layer. The findings indicate that the PV parameters are optimized when defect density is reduced to a minimum. The FF, J_{SC}, V_{OC}, and η are 81.97%, 26.25 mA/cm^2, 1.03 V, and 22.09%, respectively, at the lowest defect density (10^{11} cm^{-3}). To numerically simulate multiple semiconductor-layered devices, the SCAPS simulation tool was used in this study to model the device. The results provide insight into the impact of defect density on the performance of CsSnCl3-based PSCs.

Chowdhury et al. reported a record-high certified η of 24.2% in lab-grown PSCs in 2020, according to recent research by the Korean Study Institute of Chemical Technology [12]. In 2022, Hossain et al. reported a perovskite single-junction with less than 20% efficiency [13]. Ahmad et al.

showed that lead-free PSCs had an η of 20.19% [14]. This study illustrates that to obtain high efficiency; it is necessary to minimize the bulk defect density of CsSnCl3 PSCs. By using modeling applications such as SCAPS-1D, researchers have the opportunity to understand more about the factors that influence the performance of devices and work on creating more efficient solar cells [14–16]. Lead-based PSCs can be substituted by lead-free PSCs with CsSnCl3 absorber layers; this means that, in the future, sustainable and clean energy can be achieved.

2. Materials and methods

Figure 1 depicts the planned PSC architecture, consisting of glass, indium tin oxide (ITO), ETL, $CsSnCl_3$, CBTS, and Au layers. In this configuration, $CsSnCl_3$ serves as the absorber layer, playing a crucial role in determining the PV parameters due to its favorable optical absorption characteristics. Figure 2 illustrates the crystal structure of $CsSnCl_3$, while Figure 3 presents the schematic energy band diagram of the proposed PSC.

In the device architecture, ITO functions as the transparent conducting oxide (TCO), and CBTS is employed as the HTL, with glass and gold (Au) acting as the front and back contacts, respectively. The study explores three different ETL materials: WS_2, C_{60}, ZnSe, to investigate their impact on device performance. The interaction between the ETL and HTL layers significantly influences charge transport and extraction in the absorber, thereby affecting key parameters such as the V_{OC}, J_{SC}, FF, and PCE. Notably, the V_{OC} is governed by the Fermi level difference between ETL and HTL.

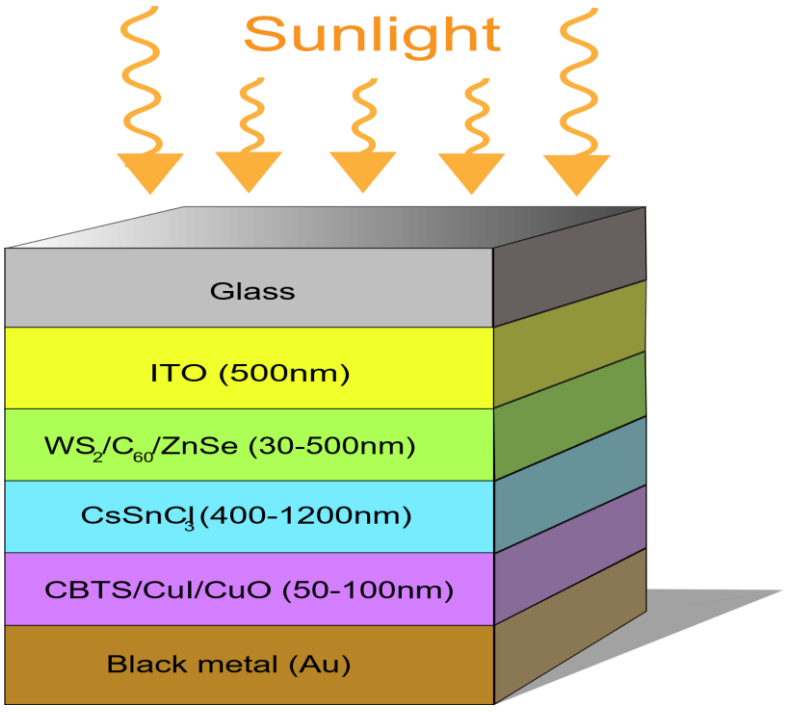

Figure 1. Design configuration of the $CsSnCl_3$-based PSC.

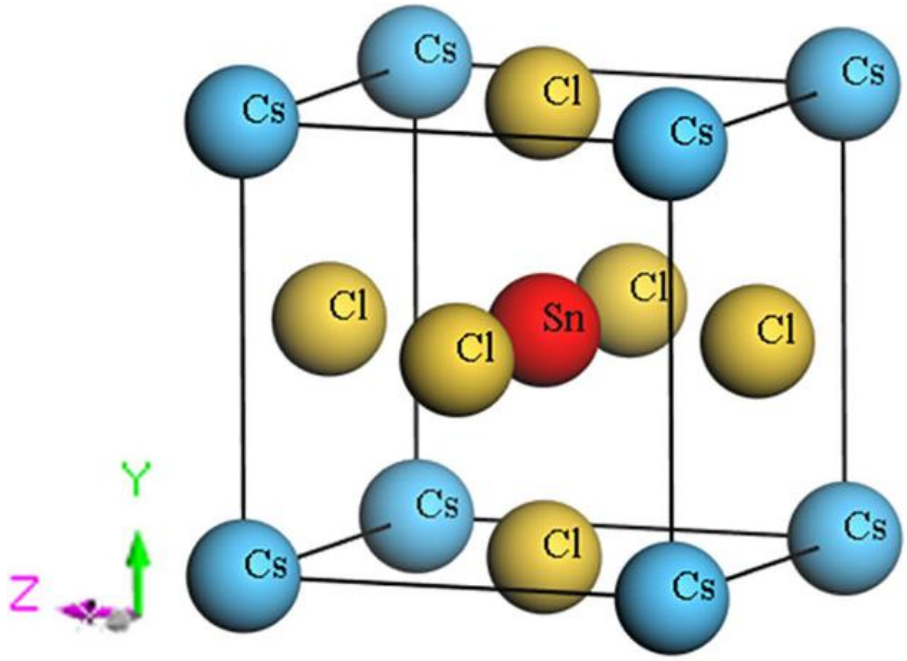

Figure 2. Optimized crystal structure of $CsSnCl_3$ perovskite.

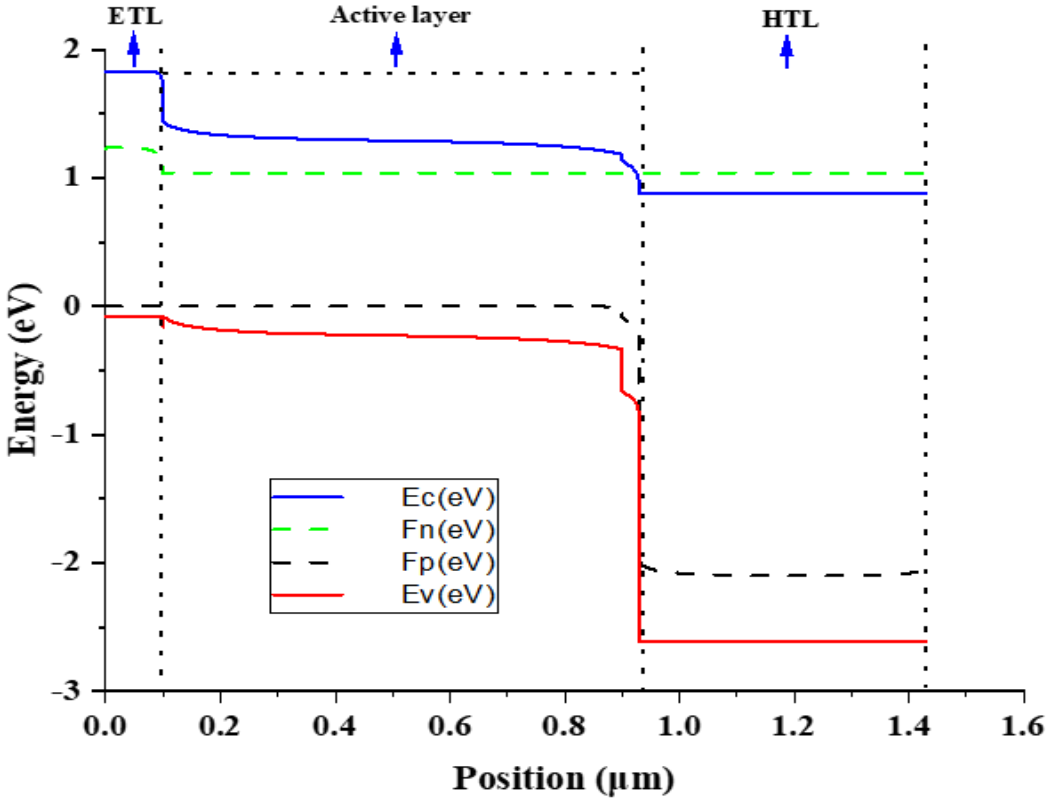

Figure 3. Schematic energy band diagram of the proposed PSC structure.

Solar cell simulations were conducted under standard illumination conditions of 100 mW/cm² using the AM1.5G solar spectrum at an operating temperature of 300 K. All simulations were performed using SCAPS-1D (Solar Cell Capacitance Simulator), a one-dimensional simulation tool developed by Burgelman and his team at the Department of Electronics and Information Systems,

University of Gent, Belgium [17,18]. SCAPS-1D is a widely used tool in PV research, capable of accurately modeling both the spectral and electrical responses of solar cells. The input parameters used for the thin-film solar cell simulations are summarized in Tables 1–3, based on data compiled from previous research studies.

Table 1. Input optimization parameters of TCO, ETL, and the absorber layer [19].

Parameters	ITO	WS_2	C_{60}	ZnSe	$CsSnCl_3$
Thickness (nm)	500	30	30	80	800
E_g (eV)	3.5	1.8	1.7	2.9	1.52
χ (eV)	4	3.95	3.9	4.09	3.9
ε_r (relative)	9	13.6	4.2	10	29.4
N_c (cm^{-3})	2.2×10^{18}	1×10^{18}	8×10^{19}	1.5×10^{18}	1×10^{19}
N_v (cm^{-3})	1.8×10^{19}	2.4×10^{19}	8×10^{19}	1.8×10^{18}	1×10^{19}
μ_n ($cm^2V^{-1}s^{-1}$)	20	100	8×10^{-2}	25	2
μ_p ($cm^2V^{-1}s^{-1}$)	10	100	3.5×10^{-3}	100	2
N_A (cm^{-3})	1×10^{21}	1×10^{18}	1×10^{17}	0	0*
N_D (cm^{-3})	0	0	0	1×10^{17}	$1\times10^{15*}$
N_t (cm^{-3})	$1\times10^{15*}$	$1\times10^{16*}$	$1\times10^{16*}$	$1\times10^{16*}$	$1\times10^{15*}$

E_g: Bandgap. **χ:** Electron affinity. **ε_r:** Dielectric permittivity. **N_c:** CB effective DOS. **N_v:** VB effective DOS. **μ_n:** Electron mobility. **μ_p:** Hole mobility. **N_A:** Shallow uniform acceptor density. **N_D:** Shallow uniform donor density. **N_t:** Defect density.

Table 2. Input optimization parameters of the HTL [19].

HTL	CuI	CuO	CBTS
Thickness (nm)	100	50	100
E_g (eV)	3.1	1.51	1.9
χ (eV)	2.1	4.07	3.6
ε_r (relative)	6.5	18.1	5.4
N_c (cm^{-3})	2.8×10^{19}	2.2×10^{19}	2.2×10^{18}
N_v (cm^{-3})	1×10^{19}	5.5×10^{15}	1.8×10^{19}
μ_n ($cm^2V^{-1}s^{-1}$)	100	100	30
μ_p ($cm^2V^{-1}s^{-1}$)	43.9	0.1	10
N_A (cm^{-3})	0	0	0
N_D (cm^{-3})	1×10^{18}	1×10^{18}	1×10^{18}
N_t (cm^{-3})	$1\times10^{15*}$	$1\times10^{15*}$	$1\times10^{15*}$

E_g: Bandgap. **χ:** Electron affinity. **ε_r:** Dielectric permittivity. **N_c:** CB effective DOS. **N_v:** VB effective DOS. **μ_n:** Electron mobility. **μ_p:** Hole mobility. **N_A:** Shallow uniform acceptor density. **N_D:** Shallow uniform donor density. **N_t:** Defect density.

Table 3. Input parameters of interface defect layers [19].

Interface	Defect type	Capture cross section: electrons/holes (cm^2)	Energetic distribution	Reference for defect energy level	Total density (cm^{-3})
ETL/$CsSnCl_3$	Neutral	1.0×10^{-17} 1.0×10^{-18}	Single	Above the VB maximum	1.0×10^{11}
$CsSnCl_3$ /HTL	Neutral	1.0×10^{-18} 1.0×10^{-19}	Single	Above the VB maximum	1.0×10^{11}

3. Results

In this study, we evaluated the PV performance of a PSC with the structure ITO/ETL/$CsSnCl_3$/HTL/Au. During simulations, the carrier concentration, thickness, and defect densities of the ETL, absorber, and HTL layers were kept constant. Specifically, the $CsSnCl_3$ absorber layer was modeled with a thickness of 800 nm, an acceptor doping concentration of 10^{18} cm^{-3}, and a defect density of 10^{15} cm^{-3}.

Our findings indicate that WS_2 and ZnSe, used as ETLs, exhibit promising results due to their wide band gaps (1.8 and 2.9 eV, respectively) and favorable electrical properties. These characteristics provide excellent transparency and suitable energy band alignment, leading to an η of approximately 22%. As shown in Table 4, among all the ETLs evaluated, the ITO/WS_2/$CsSnCl_3$/CBTS configuration delivered the highest efficiency.

Furthermore, Table 5 highlights the performance of various HTLs with the $CsSnCl_3$ absorber. CBTS emerged as the most effective HTL, achieving a PCE of around 22% due to its optimal band alignment with the absorber. In contrast, CuI and CuO-based configurations showed inferior performance. CBTS, an earth-abundant material, consistently performed well across different ETLs. Its superior characteristics—such as a unique crystalline structure, strong light absorption capability, and favorable atomic size—make it a compelling choice for HTL applications [20,21].

When sunlight strikes the device, the $CsSnCl_3$ absorber generates electron-hole pairs. Electrons, having a negative charge and typically higher mobility, are directed toward the ETL, while positively charged holes move toward the HTL. This charge separation is driven by an internal electric field, which is essential for efficient carrier collection. Since electrons have a longer diffusion length and lower recombination rate, they are more likely to reach the electrode and contribute to current generation.

Optimizing the thickness of the layers plays a vital role in improving device performance. A thicker absorber layer can capture more photons, increasing charge generation, while a thinner ETL can facilitate easier electron transport. Thus, evaluating the impact of layer thickness is critical for enhancing key performance metrics such as efficiency, FF, and J_{SC}.

3.1. Absorber layer's defect density variation effect on PV parameters

This study compared the performance of three different solar cell configurations: Cell 1 (ITO/WS_2/$CsSnCl_3$/CBTS), Cell 2, and Cell 3. Among them, Cell 1, using WS_2 as the ETL, demonstrated the best overall efficiency (approximately 25%). This high performance indicates efficient charge generation, transport, and extraction. The J_{SC} for Cell 1 was approximately 30 mA/cm²,

suggesting strong light absorption and excellent carrier mobility. It also achieved a high V_{OC} of about 1.2 V, which implies that WS_2 effectively maintains strong potential difference across the device and helps reduce charge recombination. Additionally, Cell 1 had an FF of around 80%, indicating minimal resistance losses and efficient carrier collection.

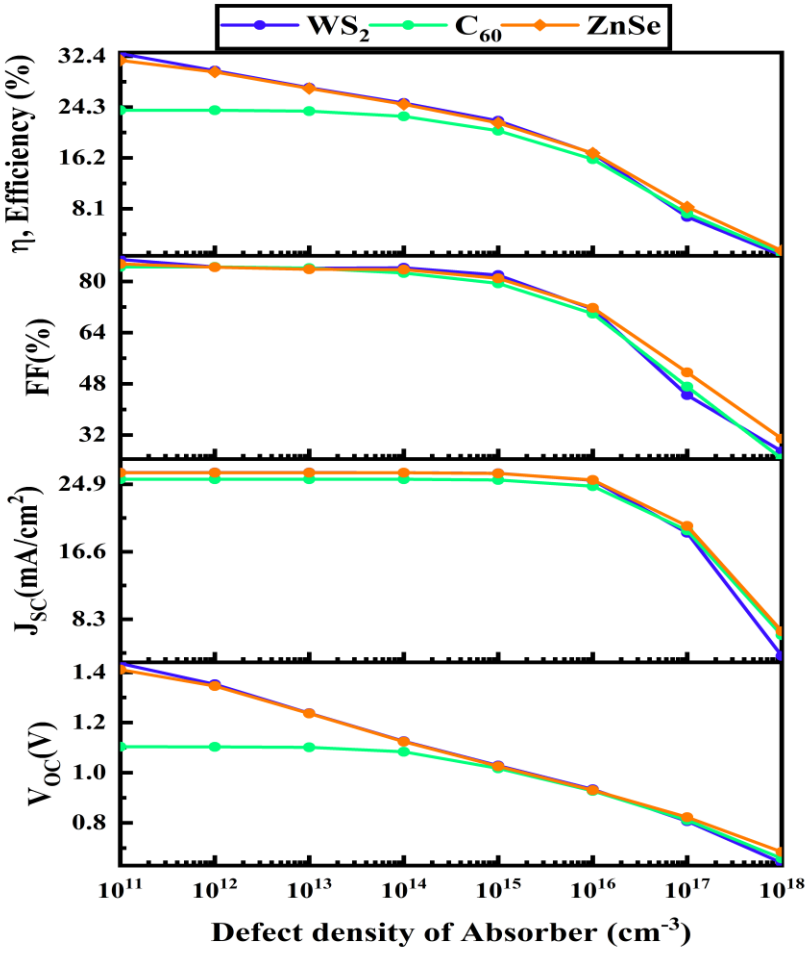

Figure 4. Absorber layer ($CsSnCl_3$) defect density variation.

Cell 2 also performed well, with an efficiency of approximately 20%, placing it in the same performance range as Cell 1, though slightly lower. It had a somewhat reduced J_{SC}, pointing to limitations in either light absorption or carrier transport. The V_{OC} was about 1.0 V (lower than Cell 1), which could be attributed to higher recombination or less effective charge extraction, possibly due to the characteristics of the C_{60} ETL used. Its FF was approximately 75%, showing moderate resistance losses and a slightly less efficient collection of charge carriers.

Cell 3 delivered the lowest performance, with an efficiency of approximately 15%. This was largely due to poor charge generation and extraction. The J_{SC} was approximately 20 mA/cm^2, suggesting suboptimal light absorption and carrier transport. Its V_{OC} was approximately 0.9 V, reflecting greater recombination losses and a weaker potential difference across the cell. The FF was also lower (approximately 70%), indicating increased resistive losses and inefficient charge collection.

In summary, among the tested ETLs, WS_2 clearly enabled the best device performance, while

ZnSe (used in Cell 3) resulted in the weakest. These comparisons and performance differences are visually summarized in Figure 4.

3.2. Absorber layer's doping density variation effect on PV parameters

Figure 5 illustrates how variations in absorber doping concentration affect the performance of PSCs, with a focus on key parameters such as FF, V_{OC}, J_{SC}, and overall PCE.

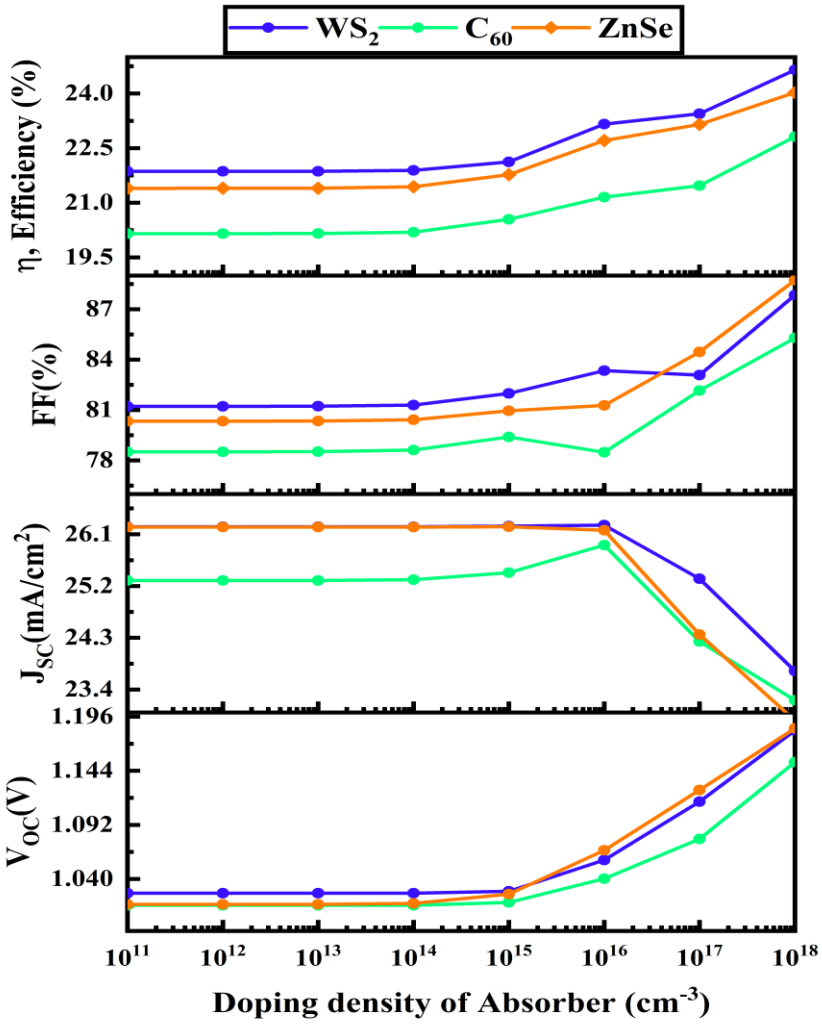

Figure 5. Absorber layer ($CsSnCl_3$) doping density variation.

The results show that increasing doping concentration generally leads to an improvement in J_{SC}. At the highest doping level of 1×10^{18} cm^{-3}, the cell with WS_2 as the ETL achieved the highest J_{SC} of 24.45 mA/cm^2, closely followed by ZnSe at 24.05 mA/cm^2. In contrast, the C_{60}-based cell exhibited a lower J_{SC}, increasing modestly from 19.69 to 21.38 mA/cm^2 as the doping concentration increased. V_{OC} behavior, however, showed a different trend. For both WS_2 and ZnSe, Voc remained relatively stable up to a doping concentration of 1×10^{15} cm^{-3}. Beyond this point, a noticeable decline occurred. WS_2 reached its peak V_{OC} of 26.25 mA/cm^2 before dropping to 23.46 mA/cm^2 at the highest doping

level, while ZnSe declined from 26.24 to 22.87 mA/cm^2. C_{60} followed a similar decreasing trend after an initial gain, though starting from a lower V_{OC}.

FF also showed modest improvement with increasing doping, especially above 1×10^{15} cm^{-3}. At the highest doping level, both WS_2 and ZnSe maintained strong V_{OC} values around 1.18 V, with FF values of 87.96% for WS_2 and 88.78% for ZnSe. C_{60}, on the other hand, peaked at an FF of 82.15%, which slightly declined at higher doping levels. These findings highlight the importance of optimizing absorber doping concentration. While increased doping can enhance J_{SC} and FF, it may also lead to a reduction in V_{OC}. Therefore, striking a balance is essential to achieving maximum overall device efficiency.

3.3. Absorber layer's thickness variation effect on PV parameters

In solar cells, increasing the absorber layer thickness generally enhances efficiency due to improved photon absorption. However, beyond a certain point—specifically beyond 1 µm—this benefit starts to diminish because of increased recombination losses. Figure 6 presents this trend clearly, showing that WS_2 delivers the highest efficiency among the ETL materials studied, peaking at 22.09% when the absorber thickness is 0.8 µm. ZnSe follows closely, achieving a maximum efficiency of 21.79% at both 0.8 and 1.0 µm. In comparison, C_{60} shows the lowest efficiency at 0.8 µm, reaching 19.94%.

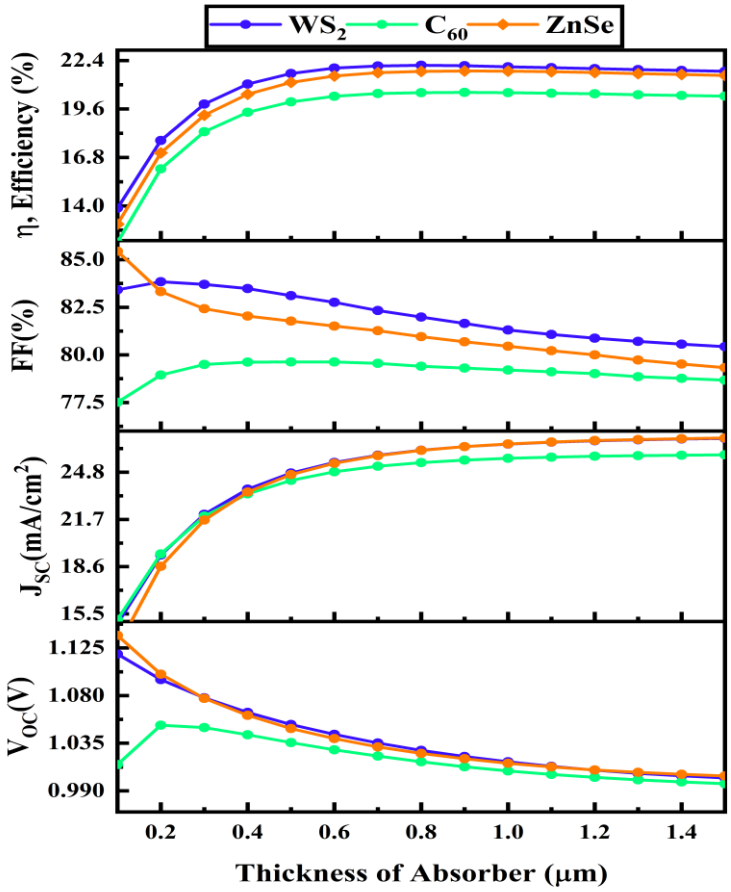

Figure 6. Absorber layer ($CsSnCl_3$) thickness variation.

As expected, J_{SC} increases with absorber thickness, due to better light absorption and more

effective charge carrier separation. At 1.2 μm, WS_2 and ZnSe both achieve peak J_{SC} values of 26.87 mA/cm² and 26.88 mA/cm², respectively, while C_{60} reaches 24.44 mA/cm².

On the other hand, V_{OC} shows a declining trend as thickness increases. For instance, WS_2 starts at a V_{OC} of 1.06 V at 0.4 μm, which drops to 1.00 V at 1.2 μm. Similar patterns are observed for ZnSe and C_{60}. This reduction may be attributed to increased resistive losses or enhanced recombination effects in thicker layers.

FF also shows a gradual decline with increasing thickness. For WS_2, FF decreases from 83.41% at 0.4 μm to 80.88% at 1.2 μm. ZnSe and C_{60} exhibit similar reductions in FF over the same thickness range.

Although thicker absorber layers help capture more light and initially boost J_{SC}, they eventually lead to diminishing efficiency returns due to a slight drop in FF and reduced improvements in J_{SC}. Thus, while J_{SC} and V_{OC} may improve up to a point, optimizing thickness is essential (beyond 0.8–1.0 μm), and the combined effects of recombination and resistive losses start to outweigh the benefits.

3.4. Optimization of ETLs (WS_2, C_{60}, ZnSe) defect density

Figure 7 illustrates how varying defect densities impact the efficiency of solar cells with different ETL materials. Notably, WS_2 and ZnSe maintained stable performance, with efficiency values holding steady at 22.09% and 21.79%, respectively, across a wide range of defect densities. In contrast, C_{60} displayed a marked decline in efficiency—from 22.10% to 19.30%—as defect density increased.

This decline is attributed to the fact that higher defect densities create more recombination centers, which hinder charge carrier collection. The data suggest that WS_2 and ZnSe are more resilient to such defect-related degradation, while C_{60} is more vulnerable. Specifically, C_{60}'s J_{SC} dropped significantly, from 26.26 to 23.05 mA/cm^2, whereas WS_2 and ZnSe showed virtually no change, maintaining stable J_{SC} values of 26.25 and 26.24 mA/cm², respectively.

Although all three materials maintained a consistent V_{OC} of 1.02 V, indicating that internal resistance and charge transport were largely unaffected by defect density, the overall efficiency trend primarily followed the behavior of J_{SC}.

FF remained steady for WS_2 and ZnSe at 81.97% and 81.00%, respectively. C_{60}'s FF declined slightly, from 81.97% to 81.93%, suggesting a minor sensitivity to increased defect density. However, the notable drop in C_{60}'s efficiency was primarily driven by reductions in both J_{SC} and, to a lesser extent, V_{OC}, rather than FF.

In summary, WS_2 and ZnSe demonstrated strong defect tolerance, maintaining high and consistent performance even as defect density increased. C_{60}, on the other hand, was significantly more sensitive to these changes, resulting in a noticeable drop in efficiency.

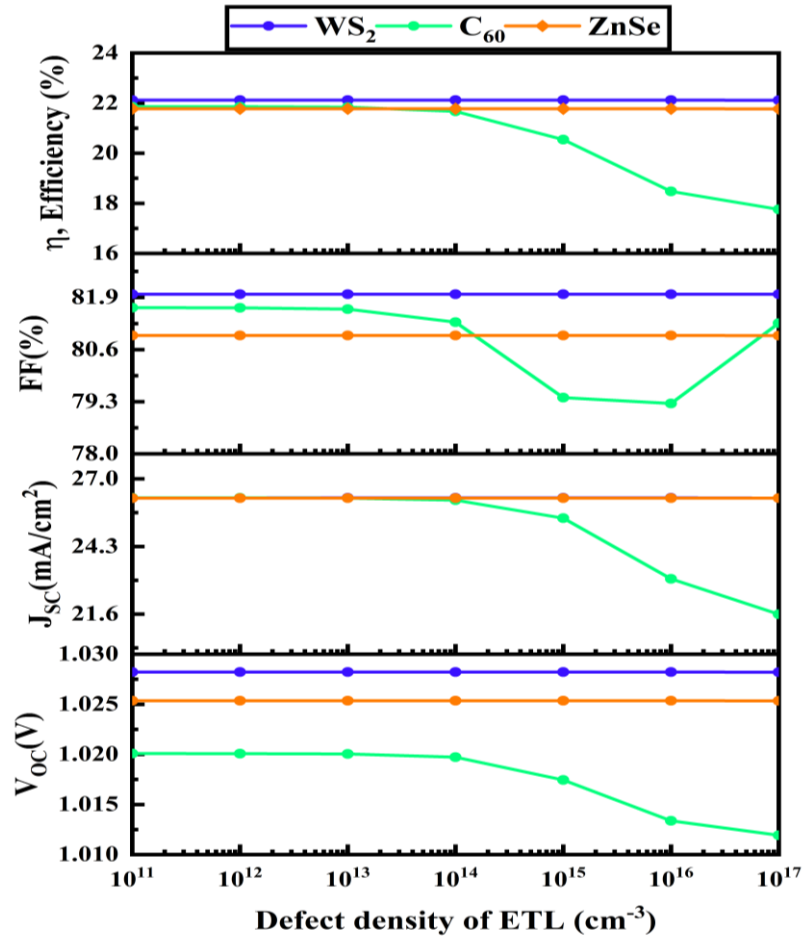

Figure 7. Defect density variation of ETLs (WS_2, C_{60}, ZnSe).

3.5. Optimization of ETL (WS_2, C_{60}, ZnSe) doping density

Figure 8 demonstrates how increasing doping concentration affects the performance of PSCs with different ETL materials. For both WS_2 and ZnSe, efficiency improves gradually as the doping concentration rises. Specifically, WS_2's efficiency increases from 22.08% to 22.17%, while ZnSe's efficiency improves from 21.80% to 22.14%. These gains are likely the result of enhanced charge carrier collection and reduced recombination losses.

In contrast, C_{60} shows a slight drop in efficiency, from 19.97% to 19.91%, which may be attributed to a decrease in charge collection efficiency due to the introduction of additional recombination sites at higher doping levels.

J_{SC} remains stable for WS_2 and ZnSe, hovering around 26.24–26.25 mA/cm^2, indicating that their charge transport is largely unaffected by increased doping. However, C_{60} sees a noticeable decline in J_{SC}, from 26.00 to 23.94 mA/cm^2, further supporting the idea that excess doping introduces recombination centers, reducing carrier mobility and potential difference.

V_{OC} stays constant at 1.02 V for both WS_2 and ZnSe. Interestingly, C_{60} experiences a slight increase in V_{OC}, from 1.01 to 1.02 V, suggesting a marginal improvement in charge separation or internal electric field strength at higher doping levels.

FF increases for all three materials with doping. ZnSe improves from 80.41% to 82.05%, while WS_2 rises from 81.97% to 82.06%. C_{60} shows the most noticeable gain in FF, increasing from 79.39% to 82.03%, which helps offset the decline in J_{SC} and maintain its overall efficiency.

In summary, higher doping concentrations lead to consistent efficiency gains in WS_2 and ZnSe, driven by improved FF and stable J_{SC} and V_{OC}. While C_{60} exhibits a drop in J_{SC}, its increasing FF and slight V_{OC} improvement help maintain a relatively stable efficiency. Among the three, C_{60} shows the most improvement in FF, but WS_2 and ZnSe remain superior in overall stability and performance at elevated doping levels.

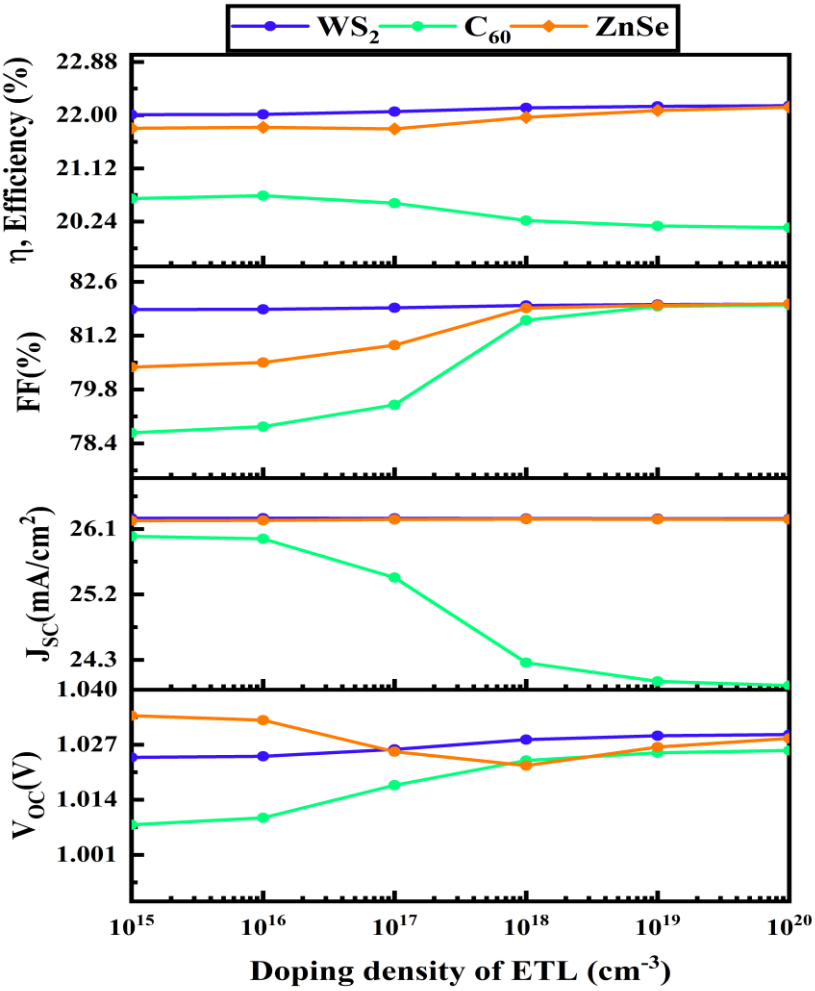

Figure 8. Doping density variation of ETLs (WS_2, C_{60}, ZnSe).

3.6. Optimization of ETL (WS_2, C_{60}, ZnSe) thickness

Figure 9 highlights how changes in ETL thickness affect the efficiency and performance characteristics of different PSCs. The results show clear differences among the materials studied.

For WS_2, efficiency gradually decreases from 22.09% at an ETL thickness of 0.03 µm to 21.69% at 0.5 µm. ZnSe, on the other hand, remains relatively stable, with only slight fluctuations between 21.82% and 21.75%. In stark contrast, C_{60} experiences a dramatic drop in efficiency—from 19.94% to

just 5.72%—as the ETL thickness increases. This sharp decline is likely due to increased resistive losses and reduced carrier mobility in thicker layers.

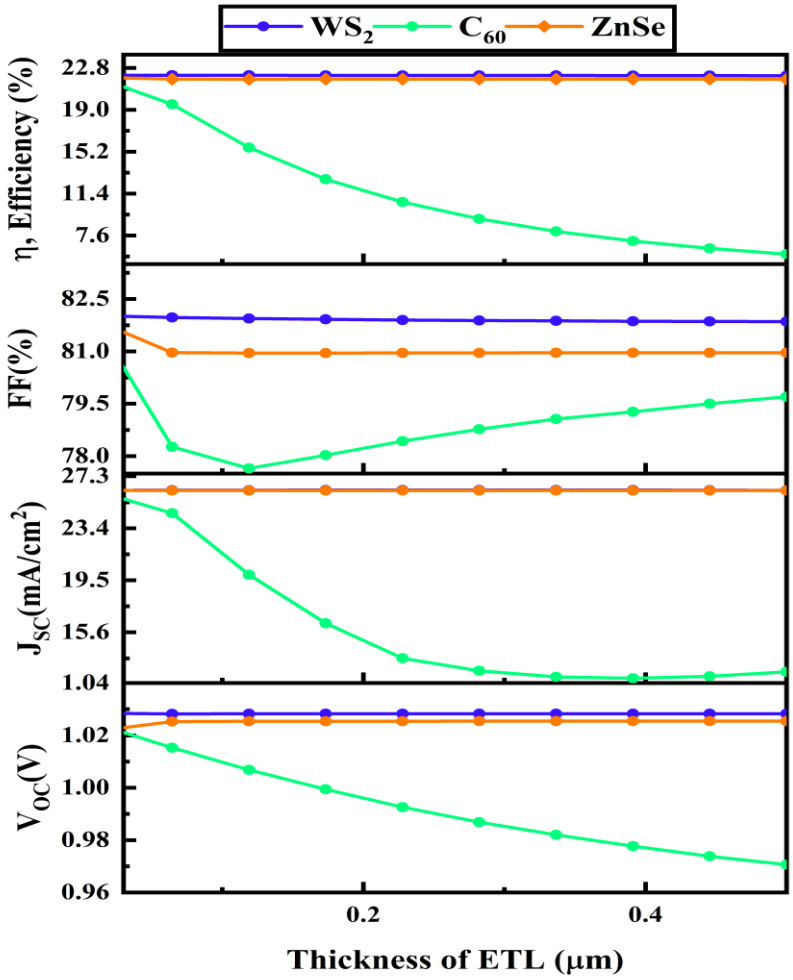

Figure 9. Thickness variation of ETLs (WS_2, C_{60}, ZnSe).

J_{SC} trends support these observations. For both WS_2 and ZnSe, J_{SC} remains nearly constant, with WS_2 ranging slightly between 26.19 and 26.29 mA/cm^2 and ZnSe dropping only marginally from 26.24 to 26.19 mA/cm^2. C_{60}, however, shows a steep decline in J_{SC}, falling from 23.85 to just 7.21 mA/cm^2 as the ETL becomes thicker, likely due to increased recombination and inefficient charge transport.

V_{OC} remains constant at 1.02 V for both WS_2 and ZnSe, indicating stable internal electric fields and good charge separation across varying thicknesses. C_{60}, however, sees a slight drop in V_{OC} from 1.02 to 0.97 V, suggesting that thicker ETLs introduce resistive losses that hinder charge collection.

FF follows similar trends. WS_2 exhibits a gradual decline in FF from 81.97% to 81.06%, while ZnSe remains stable, varying only slightly between 80.99% and 81.27%. C_{60} again shows the most significant degradation, with FF falling from 81.73% to 81.27%, driven by the combined impact of declining J_{SC} and V_{OC}.

In summary, while WS_2 and ZnSe maintain stable performance across a range of ETL thicknesses, C_{60} is highly sensitive to thickness variation. Its efficiency drops sharply due to increased resistive and

recombination losses. This highlights the importance of ETL thickness optimization, especially when using materials like C_{60}.

3.7. Defect density variation effect of HTL (CBTS)

Figure 10 illustrates that the PV performance of WS_2, C_{60}, and ZnSe-based solar cells remains unaffected across a wide range of HTL defect densities. Key performance metrics—efficiency, V_{OC}, FF, and J_{SC}—remain constant, indicating strong resilience of these materials to variations in HTL defect states.

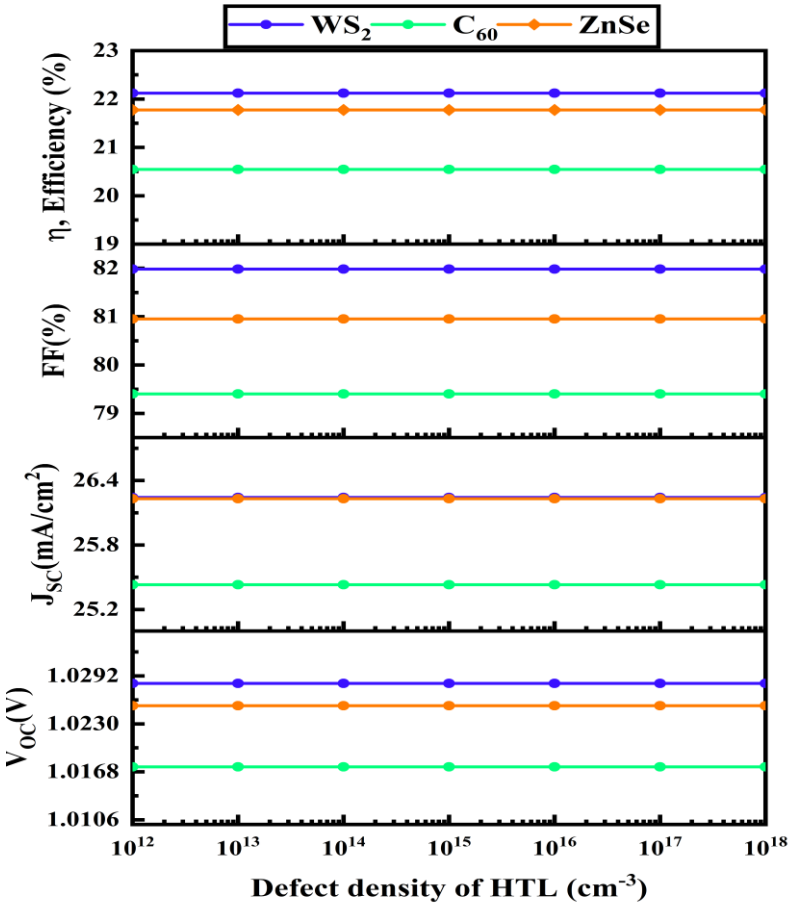

Figure 10. Defect density variation of HTL (CBTS).

WS_2 consistently maintains high performance with an efficiency of 22.09%, J_{SC} of 26.25 mA/cm², V_{OC} of 1.02 V, and FF of 81.97%. ZnSe similarly shows stable values with an efficiency of 21.79%, J_{SC} of 26.24 mA/cm², V_{OC} of 1.02 V, and FF of 81.00%. C_{60} also remains unaffected, recording 19.94% efficiency, 23.85 mA/cm² J_{SC}, and 1.02 V V_{OC} across all HTL defect densities.

These results suggest that HTL defect density has a negligible effect on the PV performance of these devices. The unchanged efficiency levels imply minimal impact from recombination losses, while the stable V_{OC} reflects consistent internal resistance and charge transport. Similarly, the unvarying J_{SC} indicates that charge separation and the built-in potential are not compromised, even at

higher defect levels.

In conclusion, the PV characteristics of WS_2, ZnSe, and C_{60} solar cells show strong tolerance to HTL defect density, reinforcing their robustness and suitability for practical device fabrication where material imperfections may be unavoidable.

3.8. Doping density variation effect of HTL (CBTS)

Figure 11 illustrates the effect of increasing HTL doping concentration on the PV performance of WS_2, ZnSe, and C_{60}-based solar cells. As doping concentration increases, all three materials show gradual improvements in efficiency, indicating enhanced charge carrier transport and reduced recombination losses.

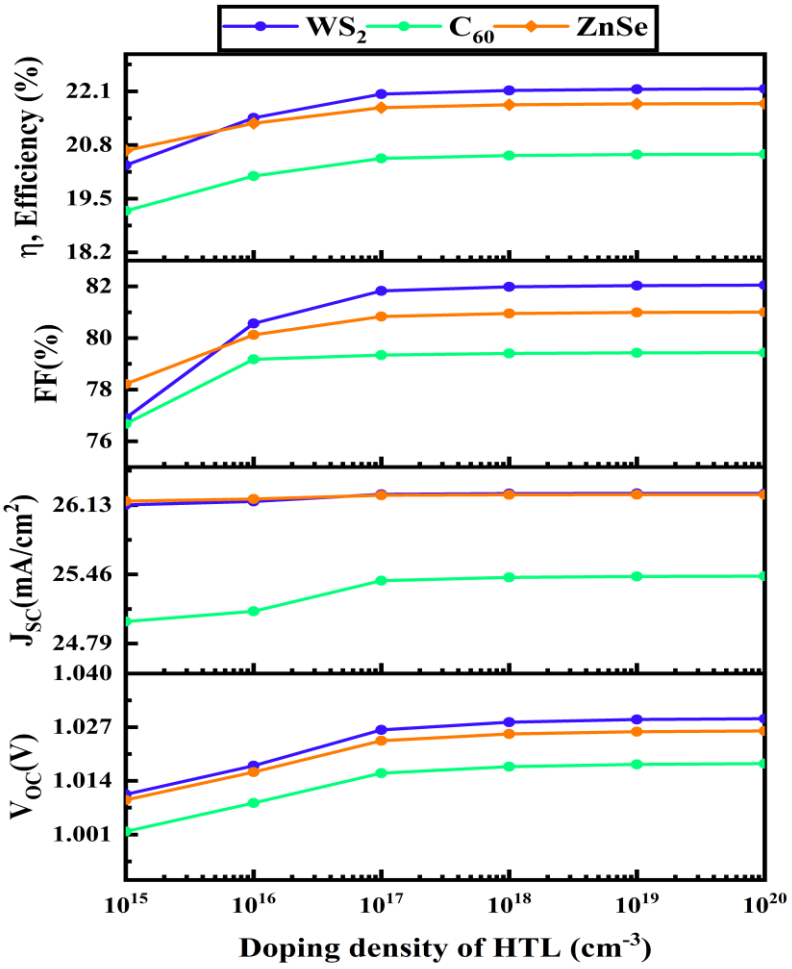

Figure 11. Doping density variation of HTL (CBTS)**.**

WS_2 exhibits the most significant efficiency gain, rising from 21.53% to 22.12%. ZnSe follows with an increase from 21.42% to 21.82%, while C_{60} shows a modest improvement from 19.43% to 19.97%. These improvements suggest enhanced charge carrier collection, particularly for WS_{60} and ZnSe, due to better built-in electric fields and reduced recombination at the HTL/absorber interface.

J_{SC} also increases slightly with higher doping levels. WS_2 improves from 26.18 to 26.25 mA/cm²,

ZnSe peaks at 26.24 mA/cm², and C_{60} increases from 23.74 to 23.85 mA/cm². These minor yet consistent gains imply more efficient charge separation and stronger built-in potentials in the device structures; again, most prominent for WS_2 and ZnSe.

V_{OC} remains constant at 1.02 V for all materials, indicating that increased doping does not introduce additional resistive losses or negatively affect charge transport properties.

FF trends mirror the overall efficiency improvements. WS_2's FF increases from 80.97% to 82.01%, ZnSe rises from 80.49% to 81.03%, and C_{60} improves from 80.86% to 81.77%. These enhancements point to lower series resistance and better charge extraction across all devices.

In conclusion, increasing HTL doping concentration leads to noticeable improvements in solar cell performance, primarily by enhancing carrier mobility and minimizing recombination. WS_2 shows the greatest performance enhancement, followed by ZnSe and C_{60}. These results highlight the importance of HTL doping optimization in achieving higher efficiency in PSCs.

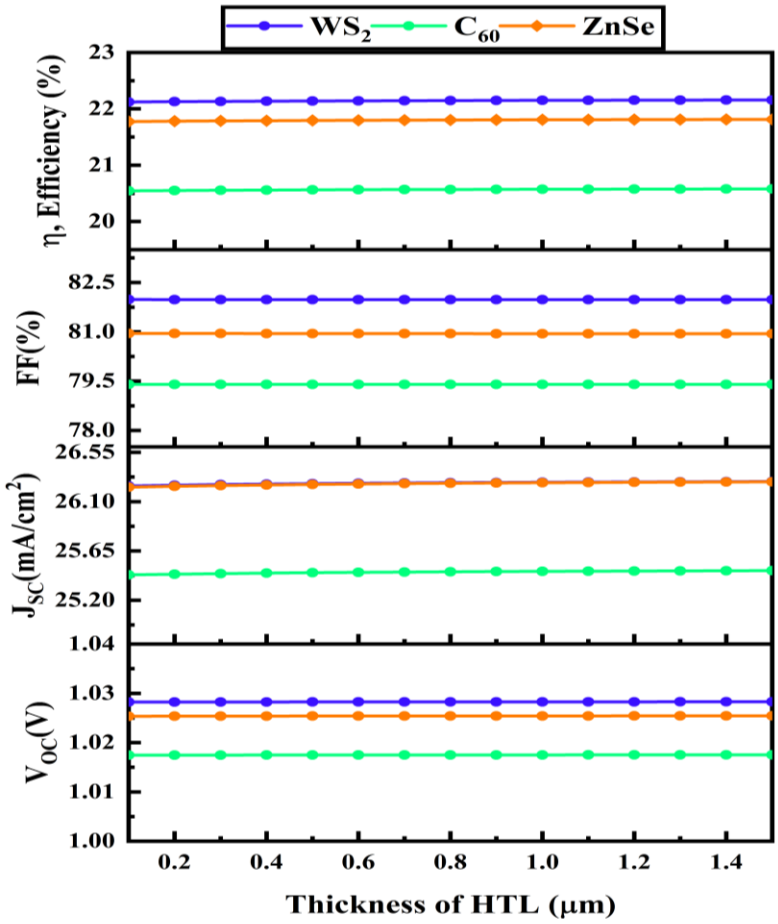

Figure 12. Thickness variation of HTL (CBTS).

3.9. Thickness variation effect of HTL (CBTS)

Figure 12 shows that the HTL thickness variation shows almost no impact on PSC performance because the HTL does not significantly influence optical absorption, built-in electric field, or recombination. Once a minimum transport thickness is ensured, further increases only cause negligible

resistance change, keeping V_{OC}, J_{SC}, FF, and η almost unchanged.

V_{OC} remains constant at 1.02 V across all HTL thicknesses and materials, indicating that internal resistance and charge transport are unaffected by HTL thickness variations.

FF also remains steady, with values around 81.73% for ZnSe, 81.97% for WS_2, and 81.00% for C_{60}. This consistency in FF, along with stable J_{SC} and V_{OC}, confirms that within the studied thickness range, HTL thickness does not significantly influence the overall PV performance of these solar cells.

3.10. Impact of capacitance and Mott–Schottky lines

Figures 13 and 14 illustrate the effects of capacitance and Mott–Schottky (M–S) behavior under an applied voltage ranging from –0.8 to 0.8 V for four different solar cell configurations. The analysis was performed at a high frequency of 1 MHz to minimize the impact of deep-level trap states.

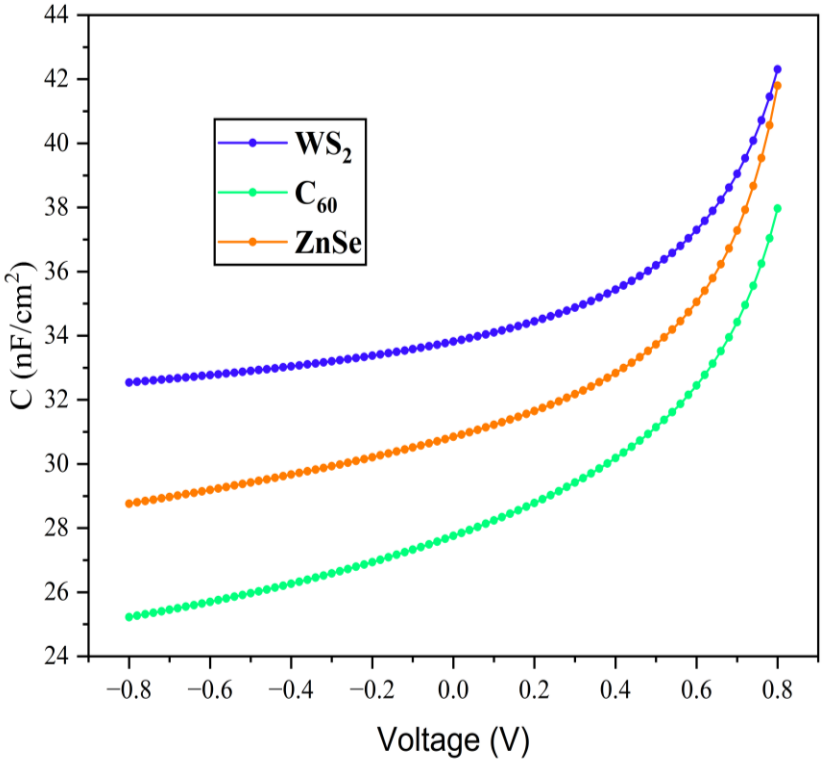

Figure 13. Capacitance–voltage characteristics of WS_2, C_{60}, and ZnSe-based devices.

As seen in Figure 13, capacitance increases exponentially with rising forward bias, indicating charge accumulation within the depletion region. The capacitance curves are nonlinear and show multiple intersections, reflecting the complex interfacial characteristics of the devices. Among the configurations, the WS_2-based ETL structure exhibits the highest capacitance at 0.8 V, while the C_{60}-based ETL shows the lowest capacitance.

This behavior suggests that under zero or reverse bias, the device operates primarily within the depletion region. As forward bias increases and the depletion width approach the absorber layer thickness, capacitance rises sharply. In contrast, under reverse bias, capacitance decreases significantly due to an increase in saturation current and widening of the depletion region. As the capacitance

increases, the interfacial recombination and resistance are reduced and there is better carrier separation, hence increasing V_{OC}, J_{SC}, FF, and efficiency.

The Mott–Schottky (M-S) plots in Figure 14 provide insights into diffusion potentials and defect densities within the devices. The slope of the $1/C^2$ versus voltage (V) curve is indicative of defect concentration: a steeper slope corresponds to lower defect density, whereas a shallower slope suggests higher trap state density. For all configurations, the M–S slope decreases with increasing voltage, consistent with previous studies, confirming the presence of interface states and the influence of applied bias on carrier dynamics. The M-S analysis further confirms that WS_2 has the lowest slope and highest built-in potential (V_{bi}), demonstrating a higher effective doping density and stronger internal electric field. The enhanced V_{bi} directly contributes to increasing V_{OC}.

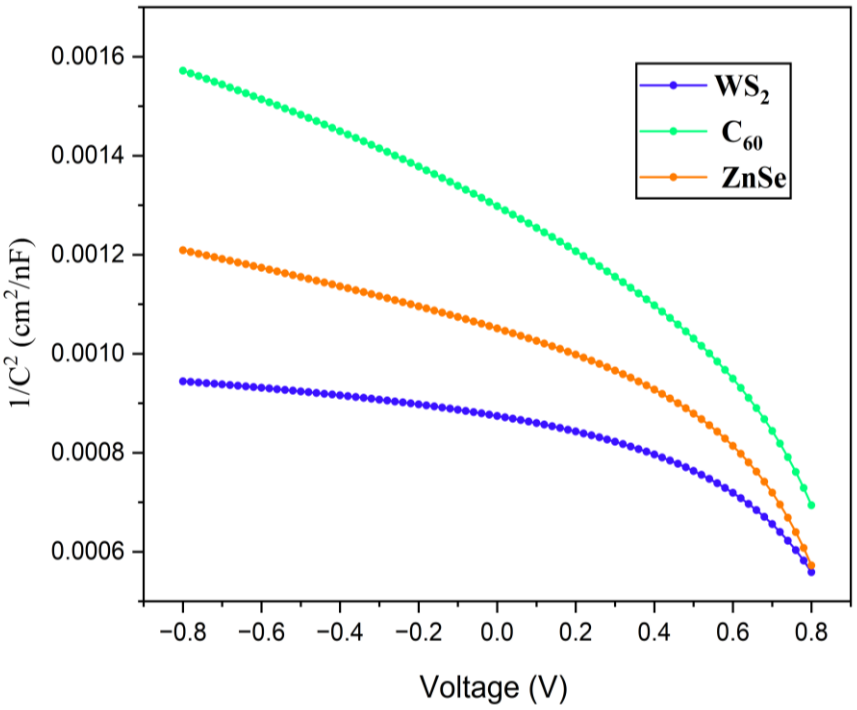

Figure 14. Mott–Schottky behavior with voltage.

3.11. Impact of generation and recombination rate

Figure 15 highlights the distinct charge carrier generation behaviors of WS_2, C_{60}, and ZnSe under varying bias voltages, providing valuable insights into their photoelectric performance. WS_2 exhibits an oscillatory generation rate, starting at 9.04 units at 0 V, dropping to 2.72 at 0.2 V, rising again to 5.88 at 0.4 V, and then declining to 2.03 at 1 V. C_{60} follows a similar pattern, beginning at 8.83, peaking at 5.76, and falling to 2.03 units. In contrast, ZnSe starts at a much lower generation rate of 1.02 units at 0 V but rises sharply to a peak of 6.18 units at 0.4 V, indicating enhanced charge generation efficiency under forward bias.

Recombination behaviors shown in Figure 16 reveal that WS_2 and C_{60} initially have high recombination rates at 0 V—2.59×10^{15} and 2.53×10^{15} units, respectively—which decrease as the bias voltage increases. ZnSe, despite having the highest initial recombination rate at 0 V (2.94×10^{15}

units), maintains more consistent and stable recombination levels at higher voltages, suggesting improved carrier extraction and reduced recombination losses under operating conditions.

Overall, WS_2 and C_{60} exhibit better performance at intermediate bias voltages, while ZnSe shows enhanced charge generation and stable recombination at higher biases. These findings suggest that each material can be optimized for specific voltage ranges to maximize PV device efficiency, supporting the development of bias-tailored solar cells.

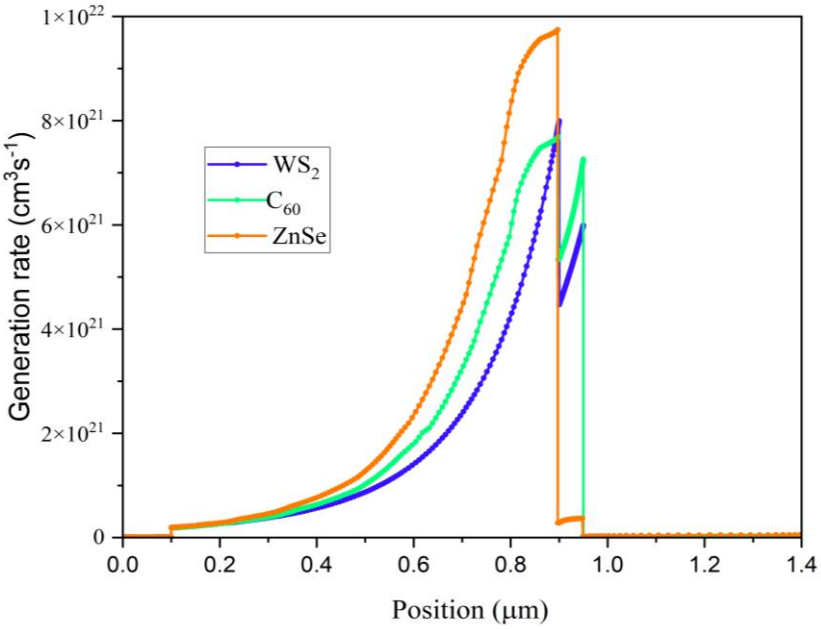

Figure 15. Generation rate profile across the thickness of WS_2, C_{60}, and ZnSe-based devices.

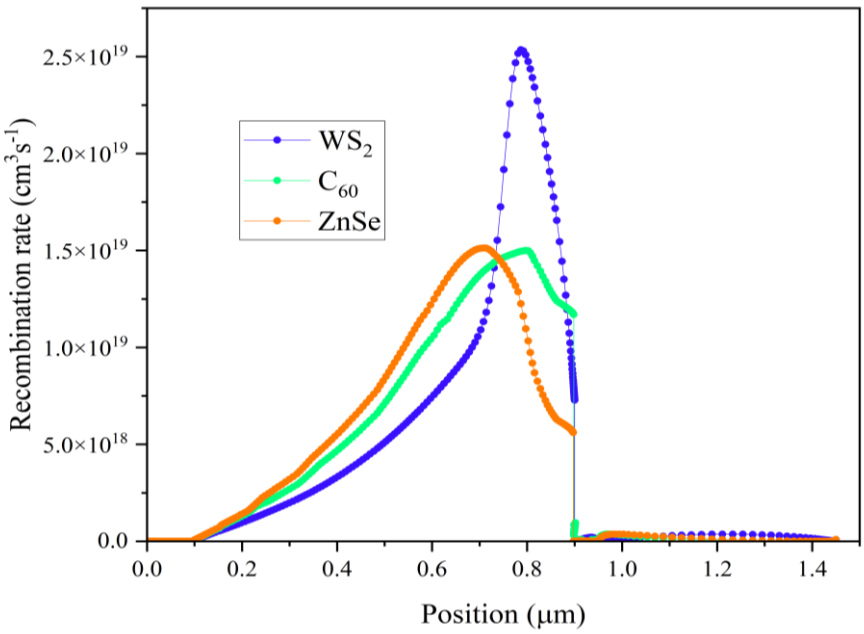

Figure 16. Recombination rate distribution in WS_2, C_{60}, and ZnSe-based devices.

3.12. Comparison of PV performance of $CsSnCl_3$ devices with different ETL and HTL materials

Tables 4 and 5 provide a comparative overview of key PV parameters for $CsSnCl_3$-based solar cells featuring different ETLs and HTLs. Table 4 reveals that among the ETLs tested, the WS_2-based device delivers the highest efficiency at 22.09%, alongside a V_{OC} of 1.03 V, a J_{SC} of 26.25 mA/cm², and an FF of 81.97%. ZnSe-based devices follow closely with an efficiency of 21.80%, while C_{60}-based devices show slightly lower performance, reaching 19.94% efficiency. Table 5 focuses on devices using WS_2 as the ETL but varying the HTL material. Here, the ITO/WS_2/$CsSnCl_3$/CBTS configuration again achieves the top efficiency at 22.09% and the highest FF at 81.97%. Devices employing CuO and CuI as HTLs show marginally reduced efficiencies of 21.98% and 20.98%, respectively. Table 6 shows the comparative analysis of our optimized device with previous published works.

Table 4. Comparison of PV parameters of $CsSnCl_3$ based on ETL.

PSC device	V_{oc} (v)	J_{sc} (mA/cm^2)	FF (%)	Efficiency (%)
ITO/WS_2/$CsSnCl_3$/CBTS	1.03	26.25	81.97	22.09
ITO/C_{60}/$CsSnCl_3$/CBTS	1.02	23.85	81.74	19.94
ITO/ZnSe/$CsSnCl_3$/CBTS	1.03	26.24	81.00	21.80

Table 5. Comparison of PV parameters of $CsSnCl_3$ based on HTL.

PSC device	V_{oc} (v)	J_{sc} (mA/cm^2)	FF (%)	Efficiency (%)
ITO/WS_2/$CsSnCl_3$/CuI	1.00	26.22	79.48	20.98
ITO/WS_2/$CsSnCl_3$/CuO	1.02	26.20	82.13	21.98
ITO/WS_2/$CsSnCl_3$/CBTS	1.03	26.25	81.97	22.09

Table 6. Comparison of our proposed device with published works.

PSC devices	V_{oc} (v)	J_{sc} (mA/cm^2)	FF (%)	Efficiency (%)	Ref.
ITO/C_{60}/$CsSnCl_3$/CBTS	1.18	22.22	87	20.5	[22]
ITO/TiO_2/$CsSnCl_3$/Cu_2O	0.67	35.7	70.68	16.94	[23]
ITO/PCBM/$CsSnCl_3$/PTAA	1.30	15.34	89.90	17.93	[19]
ITO/PCBM/$CsSnCl_3$/CBTS	1.01	25.13	80.9	20.47	[19]
ITO/WS_2/$CsSnCl_3$/CBTS	1.03	26.25	81.97	22.09	T.W.

T.W.: This work.

These results demonstrate that both ETL and HTL choices play crucial roles in determining

overall device performance. The combination of WS_2 as the ETL and CBTS as the HTL offers the most favorable balance of V_{OC}, J_{SC}, FF, and power conversion efficiency, making it the optimal configuration among those studied.

4. Conclusions

This work proposes an optimized ITO/WS_2/$CsSnCl_3$/CBTS/Au combination for a highly efficient, lead-free, and sustainable PSC based on $CsSnCl_3$. The effects of different ETL materials on device performance are evaluated. Furthermore, the performance is compared with published works. The suggested structure has an FF of 81.97%, a 26.25 mA/cm^2 short circuit current density, an efficiency of 22.09%, and a 1.03 V open-circuit voltage. We also evaluated the impacts of $CsSnCl_3$ and ETL thickness. Additionally, C–V properties, such as Mott–Schottky and capacitance, as well as quantum efficiency, J-V properties, and generation and recombination rates, were also evaluated. The structure displays superior quantum efficiency in the visible and near-infrared spectrums. Ideally, going forward, this research will contribute to the creation of solar cells devoid of lead for more adaptable and stable technology. The covalent bonding nature between Sn-Cl atoms is substantially supported by the charge density difference analysis. The maximum PCE of 22.09% with V_{OC} of 1.03 V, J_{SC} of 26.25 mA/cm^2, and FF of 81.97% was demonstrated by the WS_2 ETL and CBTS HTL-based heterojunction with ITO/WS_2/$CsSnCl_3$/CBTS/Au device configuration. PCE values for the ZnSe and C_{60}-based devices were 21.80% and 19.94%, respectively. $CsSnCl_3$ suffers from poor stability due to Sn^{2+} oxidation, moisture sensitivity, and defect formation, which limits device reliability. Future work should focus on surface passivation, alloying strategies, and encapsulation to suppress defect states and enhance long-term stability and performance of lead-free perovskite solar cells.

Use of AI tools declaration

The authors declare they have not used Artificial Intelligence (AI) tools in the creation of this article.

Acknowledgments

We express our gratitude to the Department of Electrical and Electronic Engineering at Hajee Mohammad Danesh Science and Technology University, Dinajpur-5200, Bangladesh, for their essential technical assistance.

Conflict of interest

The authors assert that there are no conflicts of interest regarding the publishing of this work.

References

1. Tota R, Tasin TI, Hasan SM, et al. (2025) Performance enhancement of lead-free K_2TiI_6-based perovskite solar cells using SCAPS-1D simulation study. *MSCE* 13: 19–37. https://doi.org/10.4236/msce.2025.1310002
2. Kishore TS, Kumar PU, Ippili V (2025) Review of global sustainable solar energy policies:

Significance and impact. *Innov Green Develop* 4: 100224. https://doi.org/10.1016/j.igd.2025.100224
3. Song Z, McElvany CL, Phillips AB, et al. (2017) A technoeconomic analysis of perovskite solar module manufacturing with low-cost materials and techniques. *Energy Environ Sci* 10: 1297–1305. https://doi.org/10.1039/C7EE00757D
4. Green MA, Ho-Baillie A, Snaith HJ (2014) The emergence of perovskite solar cells. *Nat Photon* 8: 506–514. https://doi.org/10.1038/nphoton.2014.134
5. Leijtens T, Eperon GE, Noel NK, et al. (2015) Stability of metal halide perovskite solar cells. *Adv Energy Mater* 5: 1500963. https://doi.org/10.1002/aenm.201500963
6. Saliba M, Matsui T, Domanski K, et al. (2016) Incorporation of rubidium cations into perovskite solar cells improves photovoltaic performance. *Science* 354: 206–209. https://doi.org/10.1126/science.aah5557
7. Walsh A (2015) Principles of chemical bonding and band gap engineering in hybrid organic–inorganic halide perovskites. *J Phys Chem C* 119: 5755–5760. https://doi.org/10.1021/jp512420b
8. Zaky AA, Christopoulos E, Gkini K, et al. (2021) Enhancing efficiency and decreasing photocatalytic degradation of perovskite solar cells using a hydrophobic copper-modified titania electron transport layer. *Appl Catal B Environ* 284: 119714. https://doi.org/10.1016/j.apcatb.2020.119714
9. Wu Y, Zhou J, Zhang Q, et al. (2024) Atomistic insights into optoelectronic properties of tin halide perovskite $CsSnCl_3/Cs_2SnC_{l6}$ hetero-interfaces. *Phys Letters A* 514–515: 129627. https://doi.org/10.1016/j.physleta.2024.129627
10. Banik S, Das A, Das BK, et al. (2024) Numerical simulation and performance optimization of a lead-free inorganic perovskite solar cell using SCAPS-1D. *Heliyon* 10: e23985. https://doi.org/10.1016/j.heliyon.2024.e23985
11. Green MA, Hishikawa Y, Dunlop ED, et al. (2019) Solar cell efficiency tables (Version 53). *Progress Photovolt Res Appl* 27: 3–12. https://doi.org/10.1002/pip.3102
12. Chowdhury MS, Shahahmadi SA, Chelvanathan P, et al. (2020) Effect of deep-level defect density of the absorber layer and n/i interface in perovskite solar cells by SCAPS-1D. *Results Phys* 16: 102839. https://doi.org/10.1016/j.rinp.2019.102839
13. Hossain MK, Rubel MHK, Toki GFI, et al. (2022) Effect of various electron and hole transport layers on the performance of $CsPbI_3$-based perovskite solar cells: A numerical investigation in DFT, SCAPS-1D, and wxAMPS Frameworks. *ACS Omega* 7: 43210–43230. https://doi.org/10.1021/acsomega.2c05912
14. Ahmad W, Noman M, Tariq Jan S, et al. (2023) Performance analysis and optimization of inverted inorganic $CsGeI_3$ perovskite cells with carbon/copper charge transport materials using SCAPS-1D. *R Soc Open Sci* 10: 221127. https://doi.org/10.1098/rsos.221127
15. Li H, Huang Y, Zhu M, et al. (2025) Analyzing efficiency of perovskite solar cells under high illumination intensities by SCAPS device simulation. *Nanomaterials* 15: 286. https://doi.org/10.3390/nano15040286
16. Simya OK, Mahaboobbatcha A, Balachander K (2015) A comparative study on the performance of Kesterite based thin film solar cells using SCAPS simulation program. *Superlattices Microst* 82: 248–261. https://doi.org/10.1016/j.spmi.2015.02.020
17. Burgelman M, Nollet P, Degrave S (2000) Modelling polycrystalline semiconductor solar cells. *Thin Solid Films* 361–362: 527–532. https://doi.org/10.1016/S0040-6090(99)00825-1

18. Niemegeers A, Gillis S, Burgelman M (1998) A user program for realistic simulation of polycrystalline heterojunction solar cells: SCAPS-1D, in: *Proceedings of the 2nd World Conference on Photovoltaic Energy Conversion, JRC, European Commission,* pp. 672–675.
19. Hossain MK, Toki GFI, Kuddus A, et al. (2023) An extensive study on multiple ETL and HTL layers to design and simulation of high-performance lead-free $CsSnCl_3$-based perovskite solar cells. *Sci Rep* 13: 2521. https://doi.org/10.1038/s41598-023-28506-2
20. Arumugam GM, Karunakaran SK, Liu C, et al. (2021) Inorganic hole transport layers in inverted perovskite solar cells: A review. *Nano Select* 2: 1081–1116. https://doi.org/10.1002/nano.202000200
21. Chakraborty R, Sim KM, Shrivastava M, et al. (2019) Colloidal synthesis, optical properties, and hole transport layer applications of Cu_2BaSnS_4 (CBTS) Nanocrystals. *ACS Appl Energy Mater* 2: 3049–3055. https://doi.org/10.1021/acsaem.9b00473
22. Saidani O, Yousfi A, Samajdar DP, et al. (2024) Revealing the secrets of high performance lead-free $CsSnCl_3$ based perovskite solar cell: A dive into DFT and SCAPS-1D numerical insights. *Solar Energy Mater Solar Cells* 277: 113122. https://doi.org/10.1016/j.solmat.2024.113122
23. Rawat S, Madan J (2023) Enhancing the performance and reliability of $CsSnCl_3$-based perovskite solar cells through temperature variations, in: *2023 3rd International Conference on Smart Generation Computing, Communication and Networking (SMART GENCON)*, Bangalore, India, IEEE, 1–4. https://doi.org/10.1109/SMARTGENCON60755.2023.10442687

AIMS Press